

Available online at www.sciencedirect.com

jmr&t
Journal of Materials Research and Technology

journal homepage: www.elsevier.com/locate/jmrt**Original Article****Work hardening in metastable high entropy alloys: a modified five-parameter model**

Ravi Sankar Haridas ^{a,b,c}, Priyanka Agrawal ^{a,b}, Surekha Yadav ^{a,b},
Priyanshi Agrawal ^{a,b}, Anurag Gumaste ^{a,b}, Rajiv S. Mishra ^{a,b,c,*}

^a Department of Materials Science and Engineering, University of North Texas, Denton, TX 76207, USA

^b Center for Friction Stir Processing, University of North Texas, Denton, TX 76207, USA

^c Advanced Materials and Manufacturing Processes Institute, University of North Texas, Denton, TX 76207, USA

**ARTICLE INFO****Article history:**

Received 31 December 2021

Accepted 3 April 2022

Available online 9 April 2022

ABSTRACT

Excellent work hardening in transformation-induced plasticity (TRIP)-enabled metastable high entropy alloys (HEAs) owe to persistent austenite (γ) to martensite (ϵ) phase transformation; non-basal slip activity and deformation twinning in the transformed martensitic phase are additional deformation mechanisms that contribute to work hardening in selected TRIP HEAs. Mechanical response of TRIP HEAs under uniaxial tension is characterized by an intermediate stage distinguished by a gradual increase in work hardening rate preceded and succeeded by stages of rapid drop in the work hardening rate. A five-parameter empirical model that replicates the nature of the work hardening rate curve in TRIP HEAs has been developed. The ease of parametric identification of the model from the global stress-strain response simplifies implementation of the model over physically based models. As the propensity of stress induced transformation in TRIP HEAs is related to the stacking fault energy (SFE) of the parent austenite phase, an attempt is made to correlate the model parameters with SFE. Based on the trends indicated in the correlation of model parameters with SFE as well as the initial microstructure, a method is proposed to predict the tensile stress-strain response of TRIP HEAs.

© 2022 The Authors. Published by Elsevier B.V. This is an open access article under the CC BY-NC-ND license (<http://creativecommons.org/licenses/by-nc-nd/4.0/>).

1. Introduction

High entropy alloys (HEAs) are a new class of a multi-component alloy system wherein a single phase solid solution is obtained by virtue of high entropy of mixing of constituent elements thereby eliminating the presence of any secondary phases [1]. The possibility of exploring the vast

compositional space led to the discovery of HEA compositions with synergy of excellent strength and ductility, fracture toughness, oxidation and corrosion resistance, fatigue and wear resistance, as well as high temperature properties [2,3]. In their seminal paper, Li et al. [4] demonstrated the influence of varying the elemental composition in $\text{Fe}_{80-x}\text{Mn}_x\text{Co}_{10}\text{Cr}_{10}$ HEA system on the metastability of the parent austenitic phase, thereby introducing γ (f.c.c.) $\rightarrow \epsilon$ (h.c.p.) martensitic

* Corresponding author.

E-mail address: Rajiv.Mishra@unt.edu (R.S. Mishra).

<https://doi.org/10.1016/j.jmrt.2022.04.016>

2238-7854/© 2022 The Authors. Published by Elsevier B.V. This is an open access article under the CC BY-NC-ND license (<http://creativecommons.org/licenses/by-nc-nd/4.0/>).

transformation as a strain accommodation mechanism. Subsequently, minor elemental additions such as Si, Cu, and Al in FeMnCoCr alloy system enabled metastability-driven alloy design in HEAs that resulted in excellent strength-ductility synergy via transformation induced plasticity (TRIP) [5–9]. A detailed analysis on various aspects of metastable HEAs from alloy design to deformation mechanisms was carried out by Mishra et al. [10]. Past studies on TRIP steels revealed that martensitic transformation of the retained austenite under deformation is favored when the stacking fault energy (SFE) is typically below 18 mJ m^{-2} [11]. Stacking faults in f.c.c. generally form by the glide of $\frac{1}{6}\langle 112 \rangle$ Shockley partials via dissociation of $\frac{1}{2}\langle 110 \rangle$ dislocations on {111}. An ϵ -martensitic nucleus generates in the austenitic phase when Shockley partial dissociation occurs on every other {111} plane [12,13].

Phenomenological models developed to model the mechanical behavior of TRIP steels considered the influence of microstructural features such as dislocation density, SFE, and rate of nucleation of martensitic embryos within the parent austenite [14–19]. However, these models require identification of numerous parameters through rigorous experimental procedures. Hence, empirical constitutive relations that involve easily identifiable parameters are preferred in finite element packages to overcome such tedious experimental routines. Lloyd et al. [20] proposed a work hardening-based constitutive model for medium and high Mn TRIP steels in which the work hardening behavior was approximated through a constant hardening stage followed by a rapid drop in work hardening. However, they neglected the initial stage of deformation characterized by a rapid drop in work hardening rate following yielding, which is typical of any metallic alloy and is approximated as a constant work hardening rate stage. Recently, Haridas et al. [21] proposed a four-parameter work hardening model to describe the tensile stress-strain response of TRIP HEAs in which martensitic transformation is the major strain accommodation mechanism. In the model, the work hardening curve was divided into three stages, where a constant work hardening stage separates stages of gradual drop in work hardening at the initial and final stages of deformation. Although the model could well reproduce the work hardening and tensile stress-strain responses of the metastable HEAs, further refinement of the model to replicate the exact work-hardening curve is yet possible. Though Stage II hardening is considered as a constant hardening phase, in reality, Stage II is characterized by a gradual increase in work hardening rate due to multiple deformation mechanisms occurring in the parent austenitic phase as well as transformed martensitic phase. Such a work hardening behavior is more pronounced when the initial microstructure in TRIP HEAs is dual-phased and leads to stress-partitioning; and the deformation is accommodated through slip, deformation twinning, and martensitic transformation in the parent austenitic phase; and slip and deformation twinning in the initial as well as transformed martensitic phases [6,7]. In metastable dual-phased TRIP HEAs, Sinha et al. [22] and Frank et al. [23] revealed the existence of deformation twinning and non-basal slip activity in the transformed h.c.p. martensitic phase under tensile deformation, the presence of which alters the work hardening behavior of TRIP HEAs, as mentioned

before. The present work is a refinement of our previous four-parameter work hardening model for TRIP HEAs [21] to accommodate the variation in Stage II work hardening response in dual-phase TRIP HEAs due to the synergy of multiple deformation mechanisms in both phases. Significant similarities in the modeling approach and model outcome and correlation to similarities of some of the figures and discussion within our previous model thus contribute to the authors' overall perspective concerning the present work.

2. Deformation mechanisms in metastable HEAs

Metastable HEAs are characterized by strain induced martensitic transformation under the application of load through controlling SFE of the alloy by adjusting the alloy composition as well as minor addition of other alloying elements, with resultant excellent strength and ductility [4–9]. The majority of metastable HEAs reported in literature show transformation of metastable austenitic f.c.c. phase to h.c.p. martensitic phase under deformation. The stability of the parent austenitic phase in metastable HEAs is of prominent importance when the deformation mechanisms activated under deformation are considered. Li et al. [24] demonstrated the effect of varying Mn content in $\text{Fe}_{80-x}\text{Mn}_x\text{Co}_{10}\text{Cr}_{10}$ HEA on tuning the metastability of the alloy. Varying Mn content from 45 at.% to 30 at.% resulted in a change in microstructure from a stable f.c.c. single phase to f.c.c.-h.c.p. dual phase, thereby confirming the influence of Mn content on phase constitution and stability of the parent f.c.c. austenitic phase. Later, Nene et al. [7–9] confirmed that minor addition of elements such as Cu and Al increased the stability of the austenitic phase, whereas Si reduced the stability. Further, Mishra et al. [25–27] reported that the metastability of the austenitic phase varies with compositional variation and post processing methods such as heat treatment and friction stir processing (FSP) [28]. Some recent studies have also confirmed the transformation from austenitic f.c.c. to b.c.c. martensite [29,30] as well as h.c.p. martensite to b.c.c. martensite [31] by minor addition of elements as phase stabilizers. In metastable HEAs that undergo f.c.c. to h.c.p. transformation, the deformation mechanism progresses from f.c.c. slip to h.c.p. slip (Fig. 1). The deformation starts with dislocation slip in the metastable parent austenitic phase. Further, the glide of $\frac{1}{6}\langle 112 \rangle\langle 111 \rangle$ Shockley partials via dissociation of $\frac{1}{2}\langle 110 \rangle\langle 111 \rangle$ dislocations results in the generation of stacking faults. Formation of stacking faults on every other {111} plane results in the formation of h.c.p martensitic embryo, which under further deformation results in martensitic laths through γ (f.c.c.) \rightarrow ϵ (h.c.p.) martensitic transformation [13]. With more grains undergoing transformation, stress partitioning occurs between the transformed martensitic grains and the parent austenite grains. Our previous studies reported less than ideal c/a ratio in h.c.p. martensitic phase, which evolves with processing pathways [32], alloy composition [32], strain [23,33], and strain rate [33]. c/a ratio in as-cast condition is reduced from 1.625 to as low as 1.60 in certain TRIP HEAs after tensile deformation [22].

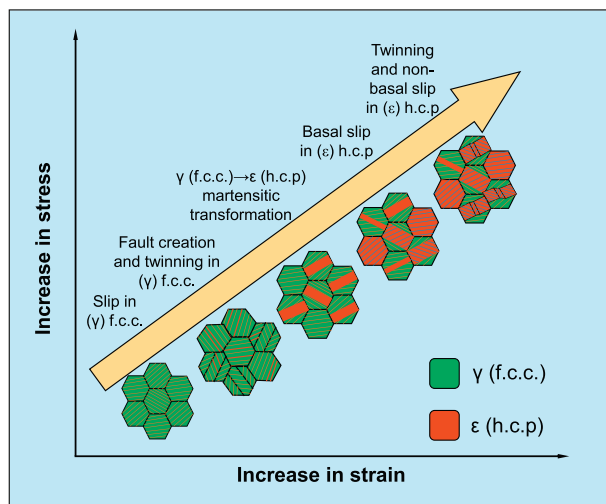


Fig. 1 – Schematic showing the progression of deformation mechanisms in metastable HEAs.

Lower c/a ratio than the ideal facilitates non-basal slip activity in addition to the common $\{0001\}\langle\bar{1}\bar{2}10\rangle$ basal slip. With the help of visco-plastic self-consistent model (VPSC) simulations, Sinha et al. [22] reported that the initial deformation stage in h.c.p. martensite is characterized by larger basal slip activity along with reasonable contribution from non-basal $\{10\bar{1}0\}\langle\bar{1}2\bar{1}0\rangle$ prismatic and $\langle c+a \rangle$ pyramidal $\{10\bar{1}1\}\langle 2\bar{1}13 \rangle$ slip activities. Further deformation results in a reduction in basal slip activity and an increase in non-basal slip activity due to variation in lattice parameters and thus excellent strength and ductility to the alloy. Additional evidence of non-basal slip activity in a metastable Fe₅₀Mn₃₀Cr₁₀Co₁₀ TRIP HEA was reported by Bu et al. [34] via in-situ TEM analysis, which accounted for more than 50% of the dislocations in the h.c.p. phase. Additionally, deformation twinning in the transformed h.c.p. martensitic phase also increases with increase in deformation, and further contributes to the excellent work hardening in TRIP HEAs. However, average active slip systems (AVACS) indicated a dominance of non-basal slip activity over twinning in the later deformation stages [22]. Using neutron diffraction technique, Frank et al. [23] reported evidence of contraction and extension twinning in h.c.p. martensitic phase. Additionally, a larger magnitude change of lattice parameter a in the early deformation stage and c in the final deformation stage evidenced the presence of dominant basal slip activity and non-basal slip activity during the initial and final deformation stages, respectively.

Figure 1 gives a general idea of the progression of the deformation mechanisms in metastable TRIP HEAs. In practice, often multiple deformation mechanisms co-exist in the bulk material in both austenitic and martensitic phases, and

depend on alloy composition, initial microstructure, grain orientation, and initial phase fraction. For example, consider a TRIP HEA with 100% f.c.c. austenitic phase subjected to tensile deformation. Those grains preferentially orientated along the loading axis favoring dislocation slip (higher Schmid factor) transform earlier than other grains with non-preferential orientation. The moment the non-preferentially oriented grains undergo twinning/slip and martensitic transformation upon further deformation, the preferentially oriented grains would progress through dislocation activity and twinning in the transformed phase. In another example, consider a dual phase alloy subjected to tensile deformation. Stress partitioning exists between both phases, and the deformation mechanisms simultaneously progress through both phases. Hence, the overall work-hardening behavior is a signature of the synergistic activity of multiple deformation mechanisms in both phases of TRIP HEAs, and thereby results in excellent alloy strength and ductility. However, sharp variations in the curvature of the work-hardening rate curve is an indication of an additional deformation mechanism to accommodate strain [20].

3. Experimental methods

Fe_{38.5}Mn₂₀Co₂₀Cr₁₅Si₅Cu_{1.5} (Cu-HEA) metastable TRIP HEA used experimentally was produced via vacuum arc melting and subsequent casting at Sophisticated Alloys Inc. Table 1 gives the nominal and actual compositions of the alloy. The cast material was further rolled to get rid of the cast microstructure. The alloy was subsequently homogenized at 1100 °C for 1 h followed by water quenching. Mini-tensile samples having a gauge length of 5 mm and cross-sectional area of $1.25 \times 1.25 \text{ mm}^2$ were milled out from the homogenized Cu-HEA plate. Uniaxial tensile tests were performed on a custom-made mini-tensile experimental setup equipped with a 500 lbs load cell at an initial strain rate of 10^{-3} s^{-1} . Samples for electron backscatter diffraction (EBSD) analysis were polished to 0.02 microns using colloidal silica. Microstructural characterization using EBSD was performed in a FEI Nova Nano SEM 230 equipped with a Hikari Super EBSD detector functioning at an operating voltage of 20 kV. TEAM® software was used for data acquisition of EBSD data; post analysis of the data was carried out in OIM TSL 8 software. Sample for TEM was prepared using FEI Nova 200 NanoLab Dual Beam Focused Ion Beam (FIB)/Field Emission Scanning electron microscope (FE-SEM) equipped with platinum gun injection system (Pt-GIS). A FEI Tecnai G2 F20 S-Twin 200 keV FE-STEM microscope equipped with Precession Electron Diffraction (PED) setup was used to obtain TEM-based OIM information. TOPSPIN software with ASTAR hardware was used for data acquisition and analysis.

Table 1 – Alloy composition of as-received Cu-HEA.

Alloy	Elements at.%	Fe	Mn	Co	Cr	Si	Cu
Cu-HEA	Nominal (%)	38.5	20	20	15	5	1.5
	Actual (%)	38.9 ± 1.1	20.1 ± 1.2	20.4 ± 1.3	14.2 ± 1.2	4.8 ± 1.5	1.6 ± 1.0

4. Results

4.1. Work hardening model

Excellent hardening in metastable TRIP HEAs is attributed to persistent γ (f.c.c.) $\rightarrow \epsilon$ (h.c.p.) martensitic transformation [4–9]. After homogenization, Cu-HEA is characterized by 100% γ (f.c.c.) phase (Fig. 2 (a1) and 2 (b1)). Upon deforming the sample to 10% axial strain under tension, martensitic transformation accounted for 22% of the deformed microstructure (Fig. 2 (a2) and 2 (b2)). Figure 2 (c) shows the true stress-strain response and the work hardening rate curve of homogenized Cu-HEA. The sample yielded at 500 MPa and reached an ultimate tensile strength (UTS) of 1.14 GPa at a plastic strain of 27%. Based on the nature of the work hardening curve, entire stress-strain response of the TRIP HEA under tension is divided into three stages [21]. Stage I is characterized by a sharp drop in work hardening, which is dominated by slip in the parent austenitic phase. The sharp drop in work hardening rate ceases after a certain amount of plastic strain, and deformation progresses into Stage II, which is characterized by a gradual increase in the work hardening rate. A rapid change in slope of the work hardening rate curve suggests persistent TRIP and deformation twinning in Stage II that causes a gradual rise in the work hardening rate (indicated by the circle in Fig. 2 (c)). Frank et al. [23] reported the evidence of contraction twinning in a TRIP CS-HEA under tensile deformation with an associated reduction in c/a ratio from 1.619 to 1.59, using in-situ neutron diffraction. Likewise, Sinha et al. [32] also reported a reduction in c/a ratio in Cu-HEA and CS-HEA under tensile deformation with evidence of deformation twinning. However, the evidence of deformation twinning in both studies was from

either SEM-EBSD or neutron diffraction analysis. Direct evidence of deformation twinning has not yet been reported using TEM for the present alloy of interest. Using prior knowledge of deformation hypothesized in [3,22,23], TEM was performed on a sample milled out from a location near the fracture of the tensile sample to understand the deformation mechanism in the transformed h.c.p. martensitic phase. Figure 3 (a) is the virtual bright field image obtained from PED of a martensitic grain showing the presence of multiple nano-twins along with the phase map (Fig. 3 (b)) of the region indicated by a rectangle in Fig. 3 (a) and corresponding OIM superimposed on the virtual bright field image (Fig. 3 (c)). The diffraction patterns obtained from two adjacent twins indicate that both plane normals belong to $\langle\bar{1}\bar{2}\bar{1}\bar{3}\rangle$ with a misorientation angle of 67.73° (Fig. 3 (d)). From Yoo [35], the twin mode is confirmed to be a compression twin, which leads to contraction along the c-axis. Evidence of nano-twinning in the transformed ϵ (h.c.p) phase establishes the contribution of mechanical twinning to the gradual increase in work hardening during Stage II deformation in TRIP HEAs (Fig. 2 (c)).

The work hardening rate further reduces in Stage III and results in failure of the material. However, the negligible post-necking non-uniform deformation in Cu-HEA causes abrupt failure. In our previous work [21], work hardening curve was modeled using an inverse hyperbolic tangent function, which approximated Stage II hardening, with a constant hardening stage to replicate sustained work hardening due to martensitic transformation. In the present work, an additional fifth parameter is included to the previous model to accommodate the gradual increase in hardening in Stage II of deformation.

The work hardening response illustrated in Fig. 2 (c) is approximated using the following empirical function,

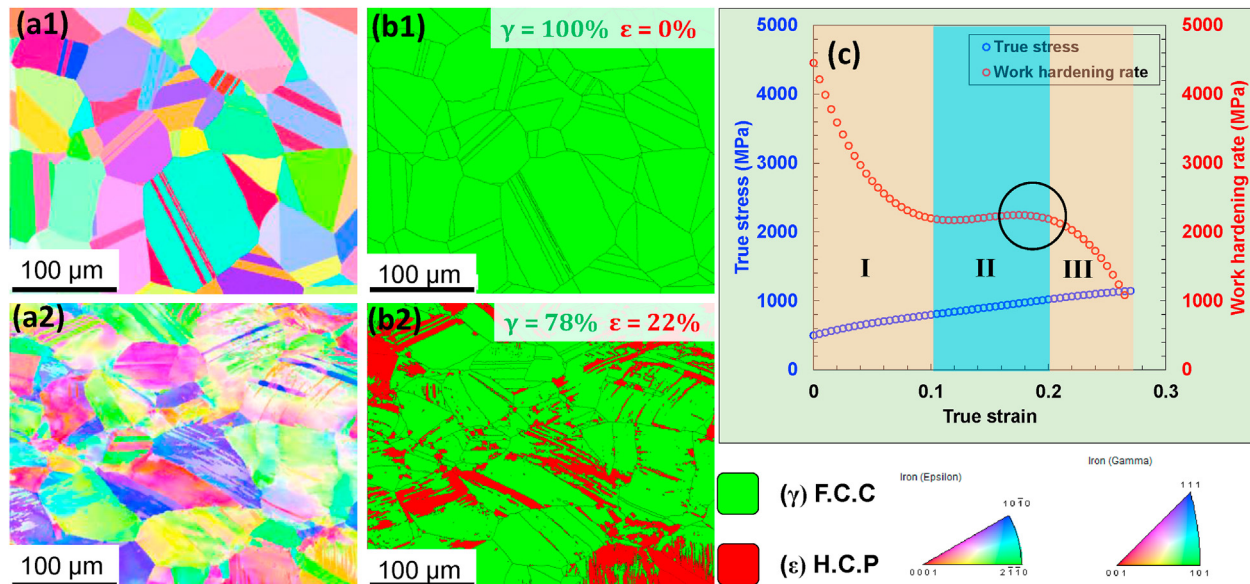


Fig. 2 – (a1) Inverse pole figure map showing the microstructure of homogenized Cu-HEA **(b1)** phase map corresponding to (a1) **(a2)** inverse pole figure map showing the microstructure of homogenized Cu-HEA deformed to 10% axial strain **(b2)** phase map corresponding to (a2), and **(c)** true stress-strain response and work hardening rate curve for as-homogenized Cu-HEA under tensile deformation.

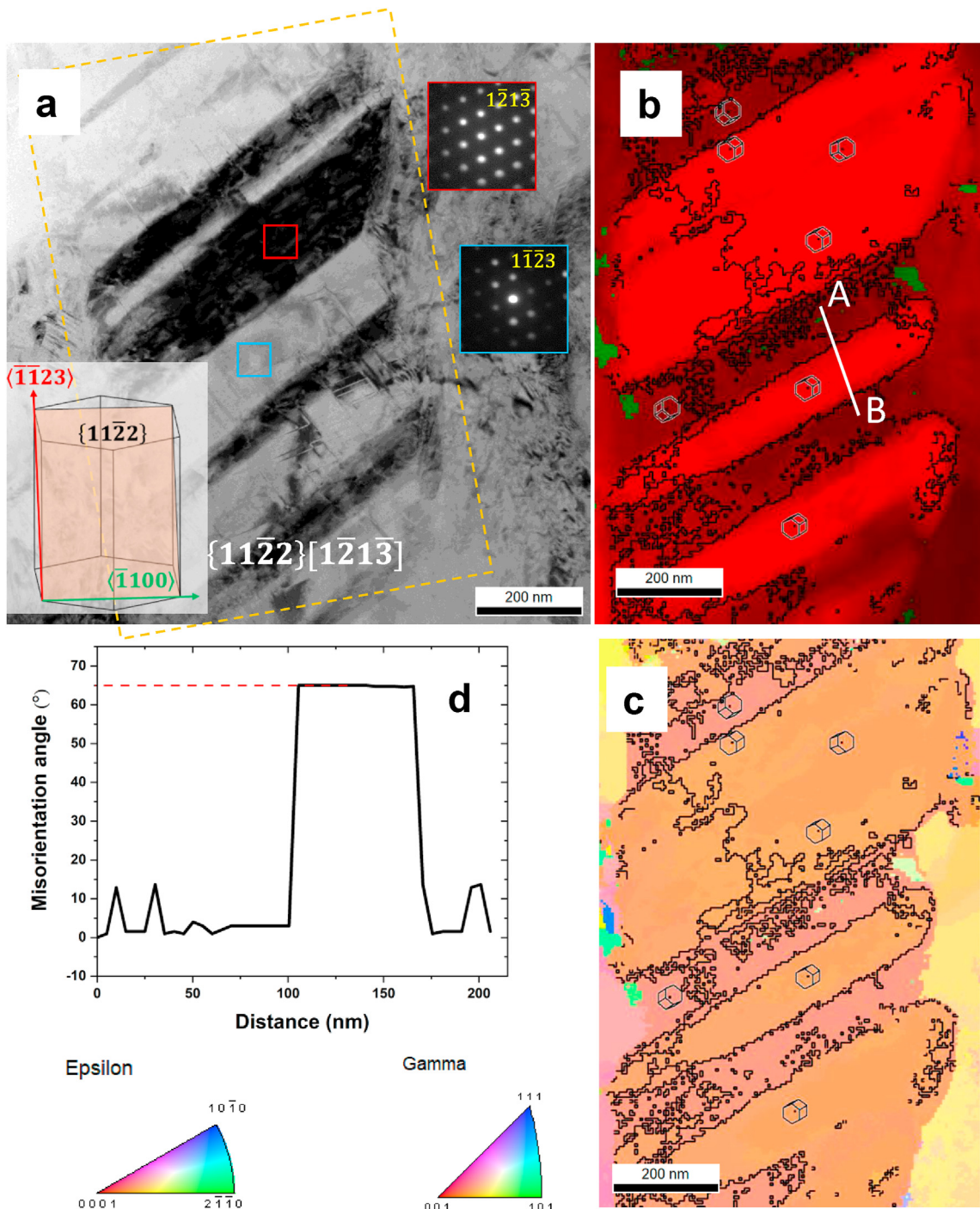


Fig. 3 – Nano-twinning in ϵ (h.c.p) phase in Cu-HEA after tensile deformation. (a) Virtual bright field image obtained from PED indicating the presence of nano-twins in the transformed ϵ (h.c.p) phase of a TEM sample prepared from a location near the fracture, **(b)** phase map superimposed on virtual bright field image at the area specified by the rectangle in (a), **(c)** corresponding orientation image micrograph (OIM) superimposed on the virtual bright field image, and **(d)** misorientation profile along the line segment AB indicated in (b) indicating a misorientation angle of $\sim 65^\circ$.

$$\frac{d\sigma}{d\varepsilon_p} = \beta_0 - \delta_1 \left\{ \left| \frac{(\varepsilon_p - \varepsilon_i)}{(\varepsilon_i + \varepsilon_e)} \right| \tanh^{-1} \left(\frac{\varepsilon_p - \varepsilon_i}{\varepsilon_i + \varepsilon_e} \right) - \delta_2 \left(\frac{\varepsilon_p - \varepsilon_i}{\varepsilon_i + \varepsilon_e} \right) \right\}, \quad \left| \frac{(\varepsilon_p - \varepsilon_i)}{(\varepsilon_i + \varepsilon_e)} \right| < 1, \quad (1)$$

where σ is the material flow stress, and ε_p is the true plastic strain that is equal to equivalent plastic strain under uniaxial

loading. Equation (1) is continuous, non-negative, and bounded in the interval $0 \leq \varepsilon_p \leq 2\varepsilon_i$. An ε_e term with a very small value of strain has been included to eliminate the unboundedness of argument of the inverse hyperbolic tangent function $\left(\frac{\varepsilon_p - \varepsilon_i}{\varepsilon_i} \right)$ at $\varepsilon_p = 0, 2\varepsilon_i$. In the current work, the model fits are obtained using $\varepsilon_e = 0.001$. Similar to our previous model,

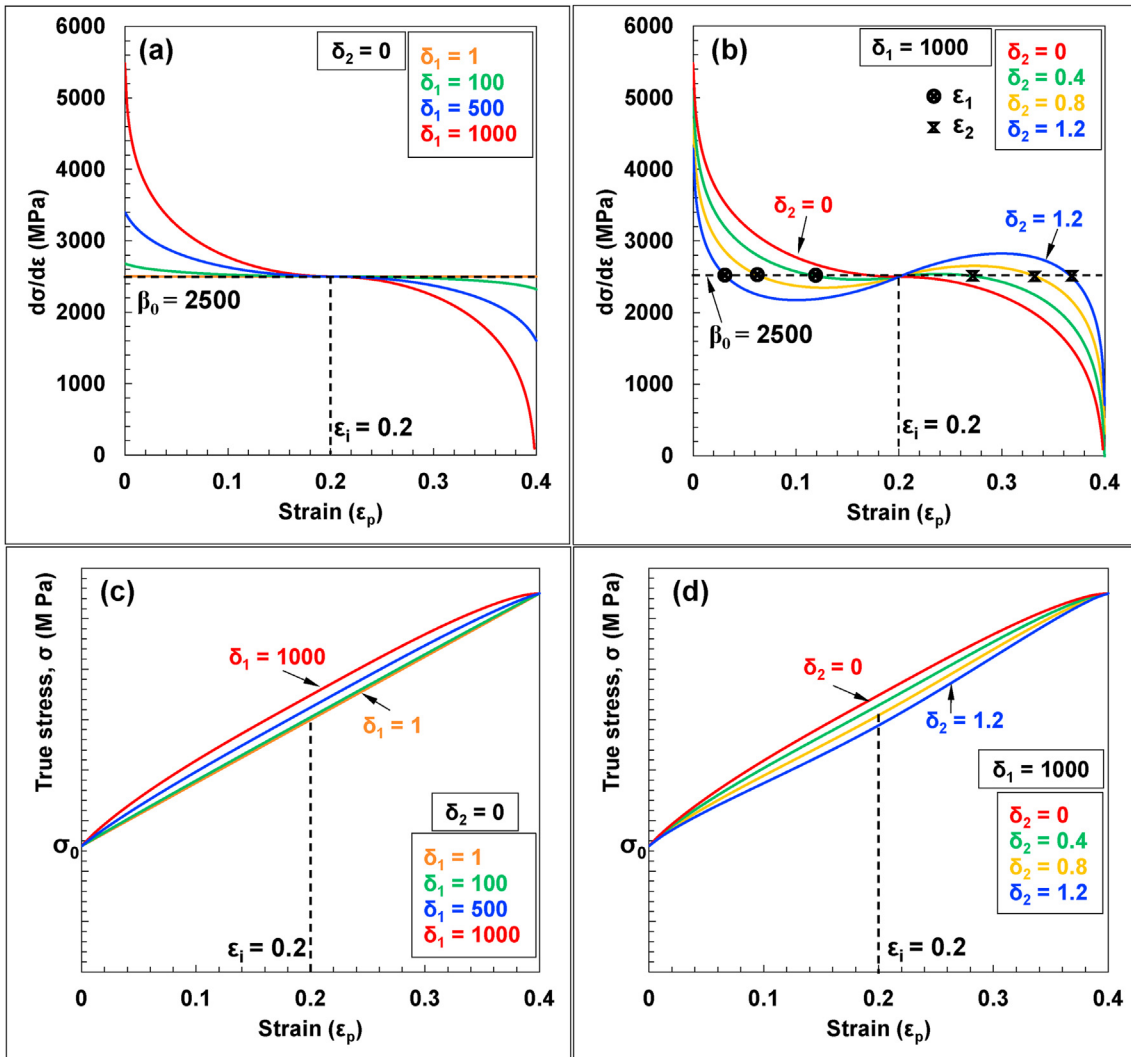


Fig. 4 – (a) Graphical representation of work hardening curves according to Eqn. (1) as a function of parameter δ_1 when the value of $\delta_2 = 0$, **(b)** graphical representation of work hardening curves according to Eqn. (1) as a function of parameter δ_2 when the value of $\delta_1 = 1000$, **(c)** true stress-strain response corresponding to the work hardening rate curves in (a), and **(d)** true stress-strain curves corresponding to the work hardening curves in (b).

parameter δ_1 controls the rate of reduction of work hardening in Stages I and III of the work hardening curve. Otherwise, δ_1 controls how abruptly $\frac{d\sigma}{d\epsilon_p} \rightarrow \beta_0$ within $0 \leq \epsilon_p \leq \epsilon_i$. β_0 is the constant work hardening rate when $\delta_1 = 0$ and corresponds to an ideal TRIP HEA which results in a linear stress-strain response from yield stress (σ_0) to failure with a constant work hardening rate. Refinement of the present model compared to the previous model [21] is accomplished through

an additional term and an additional parameter, δ_2 . Parameter δ_2 controls the gradual increase in work hardening rate in Stage II of deformation. A value of $\delta_2 = 0$ reduces Eqn. (1) to the work hardening model proposed in our previous model [21].

Equation (1) is integrated within the limits $0 \leq \epsilon_p \leq 2\epsilon_i$ to obtain the expression for flow stress as a function of ϵ_p as follows.

$$\sigma(\epsilon_p) = \beta_0 \epsilon_p \left\{ \begin{array}{l} + \delta_1 \frac{(\epsilon_i + \epsilon_e)}{2} \left(\left[(\tanh^{-1} \epsilon^*) (\epsilon^*)^2 + \epsilon^* - \ln \left| \frac{\sqrt{1 + \epsilon^*}}{\sqrt{1 - \epsilon^*}} \right| \right] + \delta_2 (\epsilon^*)^2 \right), \quad (\epsilon_p < \epsilon_i) \\ - \delta_1 \frac{(\epsilon_i + \epsilon_e)}{2} \left(\left[(\tanh^{-1} \epsilon^*) (\epsilon^*)^2 + \epsilon^* - \ln \left| \frac{\sqrt{1 + \epsilon^*}}{\sqrt{1 - \epsilon^*}} \right| \right] - \delta_2 (\epsilon^*)^2 \right), \quad (\epsilon_p \geq \epsilon_i) \end{array} \right\} + C, \quad (2)$$

where $\epsilon^* = \frac{(\epsilon_p - \epsilon_i)}{(\epsilon_i + \epsilon_e)}$ is the argument of the inverse hyperbolic tangent function in Eqn. (1). ϵ_i is half the value of the upper bound of the work hardening rate function given in Eqn. (1), and is the point of antisymmetry of the work hardening rate curve (Eqn. (2)). Integration constant C is determined using the initial condition $\sigma(0) = \sigma_0$ as follows,

$$C = \sigma_0 - \delta_1 \frac{(\epsilon_i + \epsilon_e)}{2} \left[\left(\tanh^{-1} \left(\frac{(-\epsilon_i)}{(\epsilon_i + \epsilon_e)} \right) \left(\frac{(-\epsilon_i)}{(\epsilon_i + \epsilon_e)} \right)^2 + \frac{(-\epsilon_i)}{(\epsilon_i + \epsilon_e)} - \ln \left| \frac{\sqrt{1 - \frac{(\epsilon_i)}{(\epsilon_i + \epsilon_e)}}}{\sqrt{1 + \frac{(\epsilon_i)}{(\epsilon_i + \epsilon_e)}}} \right| \right) + \delta_2 \left(\frac{(-\epsilon_i)}{(\epsilon_i + \epsilon_e)} \right)^2 \right]. \quad (3)$$

The values of five parameters σ_0 , β_0 , δ_1 , δ_2 , and ϵ_i are optimized to obtain the best fit for the stress-strain response of TRIP HEAs.

4.2. Model parameters: influence and control

The impact of each model parameter on the work hardening rate as well as the corresponding true stress-strain response is explored in the present section. The parameter σ_0 is the yield strength of the material that is dependent on alloy composition, initial microstructure, dislocation density, and initial phase fraction. Model parameter β_0 signifies constant work hardening rate when parameters δ_1 , $\delta_2 \rightarrow 0$ for $\epsilon_p \geq 0$. Work hardening curve with a constant β_0 specifies an ideal TRIP HEA, which hardens linearly from yield strength (σ_0) to failure at a constant rate of hardening. For the present analysis, values of σ_0 , β_0 , and ϵ_i have been assumed as 500 MPa, 2500 MPa, and 0.2, respectively. Figure 4 (a) shows the effect of parameter δ_1 on the work hardening response when the value of $\delta_2 = 0$. As mentioned before, as $\delta_2 \rightarrow 0$, the model reduces to our previous work hardening model where Stage II is characterized by a constant work hardening rate [21]. As evident from Fig. 4 (a), an increase in the value of δ_1 increases the rate of reduction in work hardening during Stages I and III of deformation. Also, the magnitude of work hardening rate increases with increase in value of δ_1 and decreases with increase in value of δ_1 for a specific strain in Stages I and III, respectively. Additionally, a higher value of δ_1 reduces the span of the constant work hardening rate during Stage II deformation. Hence, parameter δ_1 controls the rate of reduction of the work hardening rate in Stages I and III during deformation. Specifically, $\frac{d\sigma}{d\epsilon_p} > \beta_0$ for $\epsilon_p < \epsilon_i$ and $\frac{d\sigma}{d\epsilon_p} < \beta_0$ for $\epsilon_p > \epsilon_i$. Figure 4 (c) shows the true stress-strain response corresponding to the work hardening rate curves shown in Fig. 4 (a). Clearly, the true stress-strain curve shifts upwards with increase in value of δ_1 for $0 < \epsilon_p < 2\epsilon_i$. Otherwise, the magnitude of stress increases with an increase in the value of δ_1 for a specific strain (not inclusive of $\epsilon_p = 0, 2\epsilon_i$) and is attributed to higher magnitude of work hardening rate at large value of δ_1 during Stage I of deformation.

Figure 4 (b) demonstrates the effect of parameter δ_2 on the work hardening nature for a constant value of $\delta_1 = 1000$. The higher the value of δ_2 , the steeper the work hardening rate

curve in Stages I and III (Fig. 4 (b)). Additionally, for $\delta_2 > 0$, the work hardening rate curve falls below the curve $\beta_0 = 2500$ MPa for $\epsilon_p < \epsilon_i$ and rises above $\beta_0 = 2500$ MPa for $\epsilon_p > \epsilon_i$, thus resulting in a gradual increase in work hardening rate during Stage II deformation. Also, with an increase in the value of δ_2 , the extent of rise and fall of the work hardening curve above

and below $\beta_0 = 2500$ MPa increases. Hence, parameter δ_2 controls the rate of gradual increase in work hardening rate during Stage II deformation. Figure 4 (d) shows the true stress-strain response corresponding to the work hardening rate curves in Fig. 4 (b). Contrary to the effect of δ_1 on true stress-strain response as in 4 (c), the curve shifts downwards with increase in the value of δ_2 . Otherwise, at a constant δ_1 , the magnitude of stress decreases with an increase in the value of δ_2 for a specific strain (not inclusive of $\epsilon_p = 0, 2\epsilon_i$) that is attributed to a steeper work hardening rate during Stage I deformation followed by a drop in the work hardening rate below $\beta_0 = 2500$ MPa for $\epsilon_p < \epsilon_i$. Physically, one can interpret from the results in Fig. 4 (c) and 4 (d) that material toughness increases with an increase in value of δ_1 and a decrease in value of δ_2 , when all other model parameters are kept constant.

It is important to analyze the nature of the points on the work hardening curve at which the work hardening rate falls below and rises above $\beta_0 = 2500$ MPa, since the work hardening response between these points differentiates the present model from our previous model [21]. In Fig. 5 (a), ϵ_1 and ϵ_2 correspond to the strains at which the work hardening rate falls below β_0 for $\epsilon_p < \epsilon_i$ and rises above β_0 for $\epsilon_p > \epsilon_i$, respectively. The solutions to ϵ_1 and ϵ_2 are obtained by equating Eqn. (1) to β_0 , as follows,

$$\epsilon_1 = (\epsilon_i + \epsilon_e) \tanh(-\delta_2) + \epsilon_i, \text{ and} \quad (4)$$

$$\epsilon_2 = (\epsilon_i + \epsilon_e) \tanh(\delta_2) + \epsilon_i.$$

Importantly, ϵ_1 and ϵ_2 are functions of parameters ϵ_i and δ_2 , but independent of δ_1 . Dependence of ϵ_1 and ϵ_2 on δ_2 is evident from Fig. 4 (b) (indicated by markers), in which the value of ϵ_1 decreases and the value of ϵ_2 increases with increase in value of δ_2 . Independence of ϵ_1 and ϵ_2 on δ_1 is evident from Fig. 5 (a) in which the work hardening rate curve is plotted for multiple values of δ_1 ($\delta_1 = 100, 500, 800, 1000$, and 1500) for a constant $\delta_2 = 0.8$. Clearly, all curves intersect the line $\beta_0 = 2500$ MPa at the same $\epsilon_1 = 0.067$ for $\epsilon_p < \epsilon_i$ and at the same $\epsilon_2 = 0.33$ for $\epsilon_p > \epsilon_i$. Figure 5 (b) shows the variation of ϵ_1 and ϵ_2 as a function of δ_2 . With increase in the value of δ_2 , ϵ_1 reduces and approaches zero as $\delta_2 \rightarrow \pi$. Conversely, ϵ_2 increases with increase in δ_2 and approaches $2\epsilon_i$ as $\delta_2 \rightarrow \pi$. When Fig. 4 (b) and 5 (b) are considered together, one can

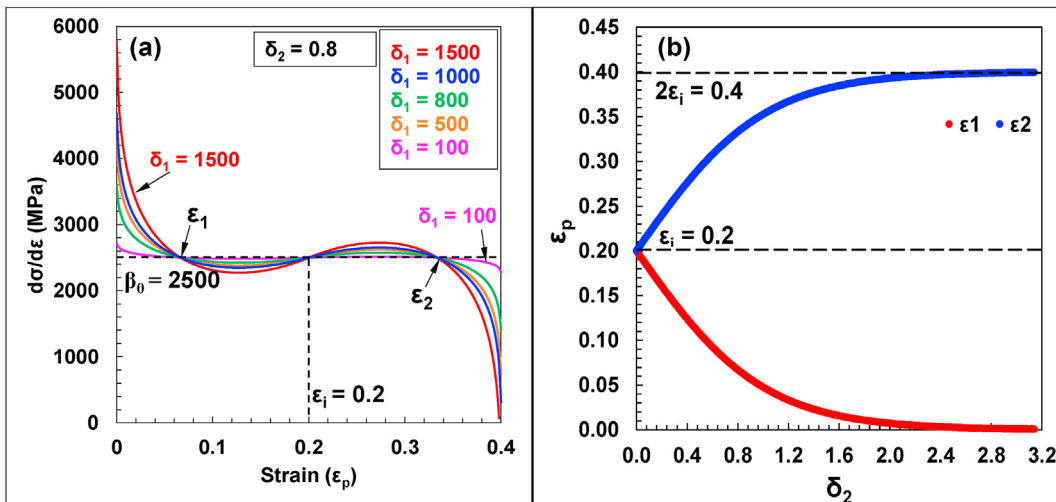


Fig. 5 – (a) Variation of work hardening rate curves for multiple values of δ_1 for a constant value of δ_2 showing independence of ε_1 and ε_2 on δ_1 , and **(b)** variation of ε_1 and ε_2 as a function of δ_2 .

conclude that a higher value of δ_2 reduces the value of ε_1 as well as increases the steepness of Stage I work hardening, and thus results in a reduction in stress in the corresponding true stress-strain curve (Fig. 4 (d)).

4.3. Considère's strain: an analysis

Considère's condition defines the strain at which uniform elongation ceases and the specimen undergoes non-uniform elongation due to necking. Considère's strain (ε_c) is the upper limit on the true stress-strain curve up to which a work hardening-based model is applicable. Beyond ε_c , non-uniform elongation creeps in due to necking, which changes the stress state in and around the necked region. A knowledge of ε_c and failure strain (ε_f) is recommended to determine the span of the total stress-strain response over which the work hardening model is applicable. ε_c is defined as the strain at which the work hardening rate equals the flow stress of the material at a particular strain rate ($\dot{\varepsilon}$),

$$\left. \frac{d\sigma}{d\varepsilon} \right|_{\dot{\varepsilon}} = \sigma, \quad (5)$$

where σ is flow stress and ε is the equivalent plastic strain. Under uniaxial tension, ε is equivalent to the true plastic strain (ε_p). Once Considère's condition is satisfied under tensile deformation, the stress state keeps changing in the necked region and deviates from the uniaxial nature. Hence, application of the work hardening model beyond ε_c is not recommended. TRIP HEAs reported in literature failed without undergoing considerable necking under tension [5–9,36,37]. Closeness of ε_f and ε_c in multiple metastable TRIP HEAs was reported [21], and the maximum elongation observed before failure once ε_c is achieved is 5%. In our previous study [21], tensile deformation of high-strength conventional alloys such as SS 316 and INCONEL 625 was compared with Cu-HEA. SS 316 and INCONEL 625 failed after undergoing profuse non-uniform deformation and necking, whereas Cu-HEA failed

abruptly, shortly after reaching ε_c . Closeness of ε_f and ε_c defines the applicability of the work hardening model for TRIP HEAs for the entire spectrum of tensile deformation from yield to failure; the aspect is discussed in the following section.

Although Eqns. (1) and (2) do not generate an analytical solution for ε_c , Fig. 6 (a) shows the numerical solution of Eqn. (5) for the modified model which demonstrates the variation of ε_c as a function of model parameter δ_1 for multiple values of δ_2 . Clearly, ε_c increases almost linearly as the value of δ_1 decreases and approaches $2\varepsilon_i$ for very low value of δ_1 . Additionally, as the value of δ_2 changes, ε_c deviates at higher δ_2 ; ε_c increases marginally with increase in value of δ_2 for a constant δ_1 . Importantly, ε_c converges to $2\varepsilon_i$ irrespective of the value of δ_2 at low values of δ_1 . At higher values of $\delta_1 > 1000$, Considère's condition being satisfied at lower strain values implies that necking occurs at an early stage of deformation. However, at low values of $\delta_1 < 500$, necking is delayed as ε_c approaches $2\varepsilon_i$. Also, Fig. 6 (b) shows the variation of ε_c as a function of δ_2 for multiple values of δ_1 . Evidently, variation in ε_c is negligible with change in the value of δ_2 for a specific value of δ_1 . Although negligible, the variation is slightly more pronounced at higher values of δ_1 compared to lower values. Furthermore, ε_c approaches $2\varepsilon_i$ at lower δ_1 values (Fig. 6 (b)). Hence, one can conclude that the influence of parameter δ_1 on ε_c is more prominent than parameter δ_2 .

5. Discussion

5.1. Model validation

Work hardening model parameters for TRIP HEAs reported in literature were identified by curve fitting the true stress-strain response in each case. To begin with, yield strength σ_0 was identified from the literature for individual HEAs. Subsequently, parameter ε_i was determined by identifying the fracture strain in each case; as an initial approximation, ε_i is considered approximately half of the fracture strain for TRIP

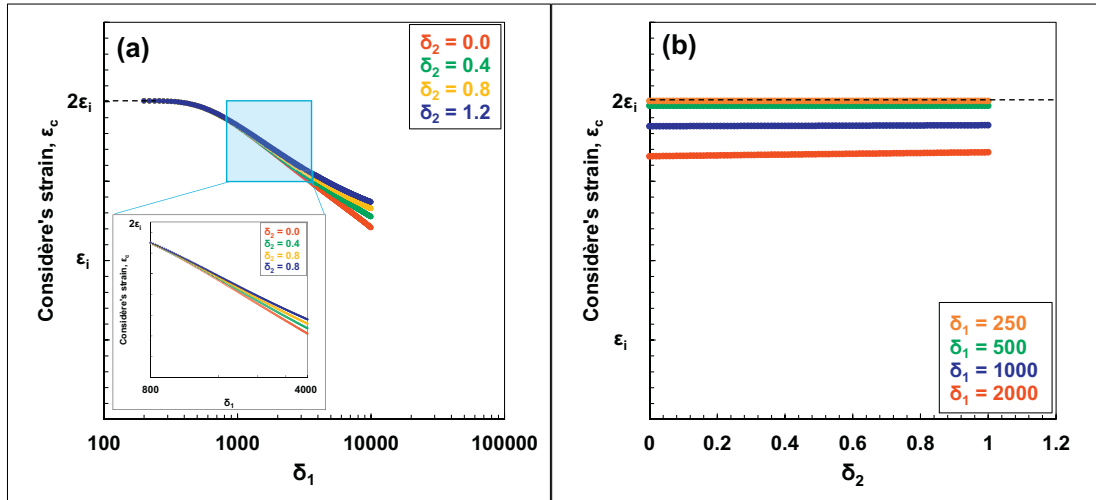


Fig. 6 – (a) Variation of Considère's strain as a function of δ_1 for multiple values of δ_2 , and **(b)** variation of Considère's strain as a function of δ_2 for multiple values of δ_1 .

HEAs [5–8]. Further, β_0 was identified by approximately matching the Stage II hardening stress. Parameter δ_2 was then determined by minimizing the least-squares error between the experimental and model true stress-strain curves in Stage II deformation. Finally, δ_1 was identified by matching the

curvature of the stress-strain response in Stage I and Stage III by minimizing the least-squares error between the experimental and model true stress-strain curves. Further error optimization between the experimental and model fit was achieved by refining the values of ϵ_i , δ_1 and δ_2 . [Figure 7](#) (a)–(c)

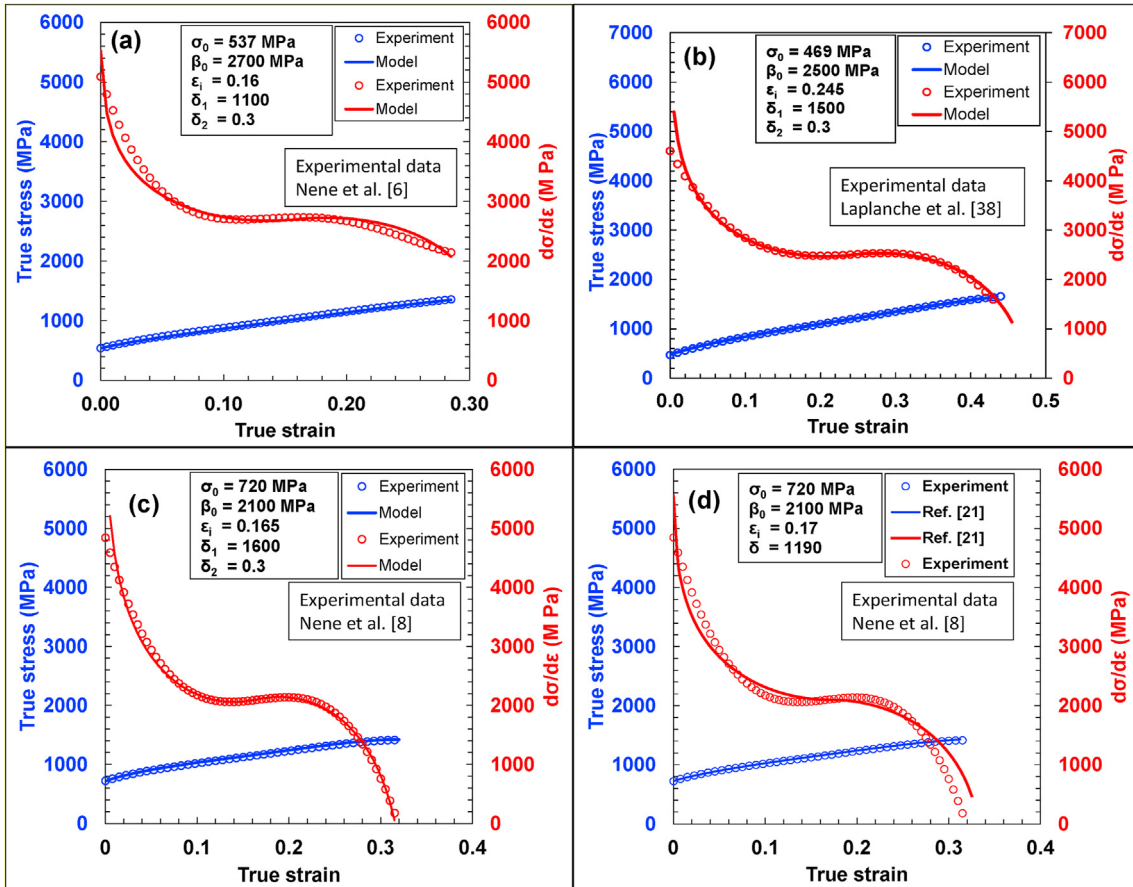


Fig. 7 – Comparison of the present model fits with experimental results, (a) Fe₃₉Mn₂₀Co₂₀Cr₁₅Si₅Al₁ HEA [6], (b) CoCrFeMnNi HEA [38], (c) Fe_{38.5}Mn₂₀Co₂₀Cr₁₅Si₅Cu_{1.5} HEA [8], and (d) four parameter model fit in Ref. [21] with the same experimental value for Fe_{38.5}Mn₂₀Co₂₀Cr₁₅Si₅Cu_{1.5} HEA [8] in (c).

Table 2 – SFE and best fit model parameters of Eqn. (1) and Eqn. (2) for various TRIP HEAs as well as medium and high Mn TRIP steels reported in literature.

SFE [mJ m^{-2}]	β_0 [MPa]	ε_i	δ_1	δ_2	σ_0 [MPa]	ε_c	ε_f	Ref.
-2.1	12,500	0.075	10,000	0.05	210	0.12	0.18	[20,39]
-1.9	6200	0.14	580	0.27	170	0.25	0.26	[20,40]
-0.7	5200	0.175	480	0.24	221	0.33	0.36	[20,40]
0.7	7100	0.09	8300	0.1	240	0.16	0.23	[20,39]
7.1	2820	0.163	1050	0.33	650	0.32	0.33	[7]
7.75	2500	0.243	1500	0.30	443	0.43	0.64	[38]
8.1	2990	0.127	600	0.29	355	0.23	0.25	[20,41]
8.9	3050	0.23	400	0.25	400	0.42	0.48	[20,41]
9.5	2450	0.27	570	0.26	508	0.41	0.45	[20,40]
10.0	3600	0.18	400	0.29	540	0.35	0.36	[11]
10.6	2450	0.285	490	0.28	325	0.52	0.58	[20,42]
13.1	2100	0.17	1900	0.30	721	0.31	0.35	[8]
13.2	2200	0.165	1200	0.25	809	0.29	0.34	[8]
13.2	2070	0.21	900	0.32	385	0.36	0.41	[5]
13.6	3200	0.173	1900	0.15	251	0.33	0.35	[5]
15.2	2670	0.16	1100	0.30	537	0.32	0.36	[6]
15.2	2320	0.175	1200	0.28	610	0.34	0.37	[6]
15.3	2800	0.145	1000	0.29	635	0.26	0.29	[6]
15.4	2330	0.215	1050	0.25	500	0.37	0.42	[6]
15.4	2510	0.195	1175	0.26	655	0.36	0.40	[6]
15.4	2650	0.165	1100	0.30	675	0.31	0.34	[6]
19.0	2450	0.26	490	0.25	240	0.53	0.54	[11]
19.9	2700	0.19	400	0.32	400	—	—	[20,41]
24.0	2050	0.285	600	0.30	345	0.53	0.60	[20,42]
29.6	2070	0.265	500	0.31	370	0.48	0.53	[20,42]
33.6	1980	0.25	460	0.30	400	0.52	0.59	[20,42]
45.8	1520	0.28	400	0.33	275	0.53	0.54	[43]

show the representative model fitting for two TRIP HEAs [6,8] and cryogenic tensile response of CoCrFeMnNi HEA [38], and indicate excellent matching with experimental results. Table 2 provides the optimized model parameters for other TRIP HEAs reported in literature and several medium and high Mn TRIP/TWIP steels with similar work hardening response. Comparison of experimental and models fits for all the alloys mentioned in Table 2 is given as supplementary data Fig. S1.

Since the current model is a refinement to our previous model, comparison of both model fits with the experimental data is important to decide how well the current model outperforms our previous model [21]. Figures 7 (c) and 7 (d) illustrate fits for the work hardening rate curve and true stress-strain curve using the current model and previous model [21], respectively, for the same TRIP HEA reported in [8]. Numerical values of the parameters employed in each model is given as inset in the corresponding figures. The proficiency of the current model to better replicate the work hardening rate curve is evident in Fig. 7 (a). However, such an appreciable variation is not evident in the true stress-strain curve between the two models since the parameters are identified by a method of error minimization between the experimental data points and the model data points on the true stress-strain curve. Still, the capability of the current model to better predict the progression of stress as a function of strain is noteworthy.

5.2. Solution to Considère's criterion: an outlook

In a previous study, Lloyd et al. [20] used a hyperbolic tangent function to describe the hardening curve for TRIP and TWIP

steels in which they neglected narrow Stage I hardening in their model by assuming that its contribution to material toughness is negligible. However, one cannot neglect Stage I deformation in TRIP HEAs since its contribution to material toughness is appreciable due to early TRIP activity (Fig. 2 (c)). As mentioned in Section 4, the hardening function described in Eqn. (1) is defined over the range $0 \leq \varepsilon_p \leq 2\varepsilon_i$. Beyond an equivalent plastic strain of $2\varepsilon_i$, the function becomes unbounded. In most of the conventional alloys, failure occurs at strain levels beyond $2\varepsilon_i$ following severe non-uniform deformation associated with necking. Accordingly, the equivalent plastic strain in the necked region is considerably higher than the nominal strain in the gauge length [20]. In such cases the model is insufficient to accommodate the extensive non-uniform elongation that exists once Considère's strain is reached until failure. In any case, the model is still an effective tool to predict the mechanical response in the uniform elongation stage until Considère's criterion is satisfied. As evident in Fig. 6 (a), for very low values of $\delta_1 < 200$, Considère's criterion fails to provide a solution due to extended Stage II hardening at such low values. Additionally, as mentioned in Section 4.1, the upper bound of the model is $2\varepsilon_i$, beyond which the function becomes unbounded. Therefore, to establish the applicability of the model during the entire uniform deformation stage in metastable TRIP HEAs, the existence of ε_c within the range $0 \leq \varepsilon_p \leq 2\varepsilon_i$ must be confirmed. A comparison of ε_i and ε_c in Table 2 for all TRIP HEAs reported in literature confirms that ε_c is well below the upper bound of the model. Thus, one can safely say that the model is capable of predicting the stress-strain response throughout the uniform deformation under tension in TRIP HEAs.

5.3. Correlation of model parameters with SFE

Methodology for determining SFE of TRIP HEAs and TRIP steels was discussed in our previous model [21] and, for completeness, the same is also described here. Description for energy to form a stacking fault formulated by Olson and Cohen [13] is used to determine SFE and to correlate with the model parameters.

$$\text{SFE} = n\rho(\Delta G_{\text{chem}}^{\gamma \rightarrow \epsilon} + E^{\text{str}}) + 2\sigma^{\gamma/\epsilon}, \quad (6)$$

where, per Olson and Cohen, $n = 2$ is the number of faulted planes that act as martensitic nuclei, ρ is the planar atomic density of the f.c.c. close packed {1 1 1} planes, which is determined as 2.97×10^{-5} mol m⁻² using the value of lattice parameter $a_{\text{f.c.c.}} = 3.5912 \text{ \AA}$ [32]; $\Delta G_{\text{chem}}^{\gamma \rightarrow \epsilon}$ is the chemical driving force for austenite-martensite transformation; $E^{\text{str}} = 22.2 \text{ J/mol}$ is energy barrier for transformation [44]; and $\sigma^{\gamma/\epsilon} = 15 \text{ mJ/mol}$ is the interfacial energy between the two phases [44]. The values of $\Delta G_{\text{chem}}^{\gamma \rightarrow \epsilon}$ for different TRIP HEAs were reported in [27,44]. Lloyd et al. [20] have demonstrated determination of SFE as a function of alloy composition and shown the compositional dependence on their model parameters as a function of SFE. Further, extrinsic dependence of grain size on stacking fault generation ($\Delta G_{\text{ex}}^{\gamma \rightarrow \epsilon}$) is considered, and is described as [45],

$$\Delta G_{\text{ex}}^{\gamma \rightarrow \epsilon} = k_1 \exp(-d/k_2), \quad (7)$$

where d is austenitic grain size, k_1 (170.06 J/mol) and k_2 (18.55 μm) were determined experimentally for TRIP steels [45]. Hence, Eqn. (1) is modified to obtain the effective SFE as:

$$\text{SFE} = n\rho(\Delta G_{\text{chem}}^{\gamma \rightarrow \epsilon} + E^{\text{str}} + \Delta G_{\text{ex}}^{\gamma \rightarrow \epsilon}) + 2\sigma^{\gamma/\epsilon}. \quad (8)$$

Effective SFE for TRIP/TWIP HEAs [5–9,38] as well as certain medium and high Mn TRIP/TWIP steels [11,20,39–43,46] having similar work hardening response are summarized in Table 2. Work hardening model parameters for the TRIP HEAs/TRIP steels summarized in Table 2 were plotted against SFE in Fig. 8 (a)–(d) to check for any possible correlation. Variation of parameter β_0 with SFE fitted well to a power law (Fig. 8 (a)). As discussed before, parameter β_0 controls the sustained work hardening during Stage II deformation of TRIP HEAs that is governed by deformation mechanisms such as martensitic transformation as well as twinning in the transformed martensitic phase, which in turn depends on SFE of the alloy [10]. Alloys with lower SFE promotes martensitic transformation at low stress levels and hence results in profuse hardening, thus justifies the trend observed in Fig. 8 (a). For example, different FSP conditions resulted in various grain refinement levels in Cu-HEA [8]; a 350 rpm run resulted in an average grain size of 7 μm whereas a 150 rpm run resulted in 0.6 μm average grain size, both having a single phase γ (f.c.c.) microstructure with martensitic transformation as the primary deformation mechanism. The effective SFE calculated as per Eqn. (8) is 10.6 mJ m⁻² and 13.2 mJ m⁻² for 350 rpm and 150 rpm runs, respectively. The optimized values of β_0 for 350 rpm and 150 rpm runs are obtained as 2450 MPa and 2100 MPa, respectively. The above result substantiates the ease of martensitic transformation in 350 rpm run as

compared to 150 rpm run owing to lower SFE in the former, which enabled higher Stage II work hardening rate and associated β_0 value. However, 150 rpm FSP of another low SFE CS-TRIP HEA (SFE = 7.1 mJ m⁻²) resulted in a dual phase microstructure with comparable average grain size [7]. The low SFE CS-HEA with a dual phase microstructure resulted in a higher Stage II work hardening ($\beta_0 = 2610 \text{ MPa}$) compared to Cu-HEA processed at same FSP conditions. Notably, the higher Stage II work hardening rate is attributed to the existence of multiple deformation mechanisms in both phases in synergy; persistent martensitic transformation in γ (f.c.c.) phase due to low SFE and deformation twinning in ε (h.c.p.) phase [7,23]. Similar observations can be made from the work of Buchely et al. on rolling of medium Mn TRIP steels [40]. Alloy with a higher SFE of 9.5 mJ m⁻² (alloy D in [40]) showed a single phase austenitic microstructure whereas the one with a lower SFE (−1.9 mJ m⁻²) (alloy C in [40]) resulted in a triple phase (γ (f.c.c.), ε (h.c.p.), and α (b.c.c.)) microstructure when subjected to hot rolling which indicates the ease of martensitic transformation in the lower SFE alloy. Such a microstructural evolution is also reflected in the stress-strain response where alloy D resulted in a lower Stage II work hardening rate ($\beta_0 = 2450 \text{ MPa}$) compared to alloy C ($\beta_0 = 6200 \text{ MPa}$). Hence, the value of β_0 strongly depends on the SFE of the alloy, initial microstructure, and the operative deformation mechanisms.

Unlike variation of β_0 with SFE, correlation of parameter ϵ_i indicated a linear trend (Fig. 8 (b)). Since $\epsilon_i \sim \epsilon_f/2$, the linear increase of ϵ_i with SFE suggests an increase in ductility with an increase in SFE. The extent of strain at which the operative deformation mechanisms become so refined that they cease to evolve with further strain, strongly depends on SFE. Lower the value of SFE, easier is the propensity for martensitic transformation which further results in saturation of martensitic transformation and deformation mechanisms at lower strain levels, leading to early failure under tension. For example, Cu-HEA and CS-HEA processed using the same FSP conditions (150 rpm) resulted in a single phase and dual phase microstructures [7,8], respectively. Cu-HEA which has a higher effective SFE (10.6 mJ m⁻²) showed extended ductility ($\epsilon_f = 32\%$) compared to CS-HEA with lower effective SFE (7.1 mJ m⁻²) ($\epsilon_f = 21\%$). Notably, prominent deformation mechanism is martensitic transformation in Cu-HEA owing to a single phase microstructure, thus extending the saturation strain for martensitic transformation due to availability of higher volume of γ (f.c.c.) phase. However, CS-HEA undergoes load sharing in both phases and attains saturation of martensitic transformation at a lower strain level due to lower SFE and lower volume of γ (f.c.c.) phase, thereby resulting in early failure. Similar behavior is also observed in TRIP steels where the alloy with lower effective SFE (−1.9 mJ m⁻²) (alloy C in [40]) failed at $\epsilon_f = 25\%$ whereas the one with higher effective SFE (9.5 mJ m⁻²) (alloy D in [40]) failed at $\epsilon_f = 45\%$. Hence, parameter ϵ_i also depends on the initial microstructure and the prominent deformation mechanism activated during deformation, as the ductility of the alloy is governed by factors such as grain size, phase volume fraction, presence of secondary phases and intermetallics, interplay of multiple deformation mechanisms, and their sequence of occurrence [10]. Further, the aforementioned micro-mechanisms depend

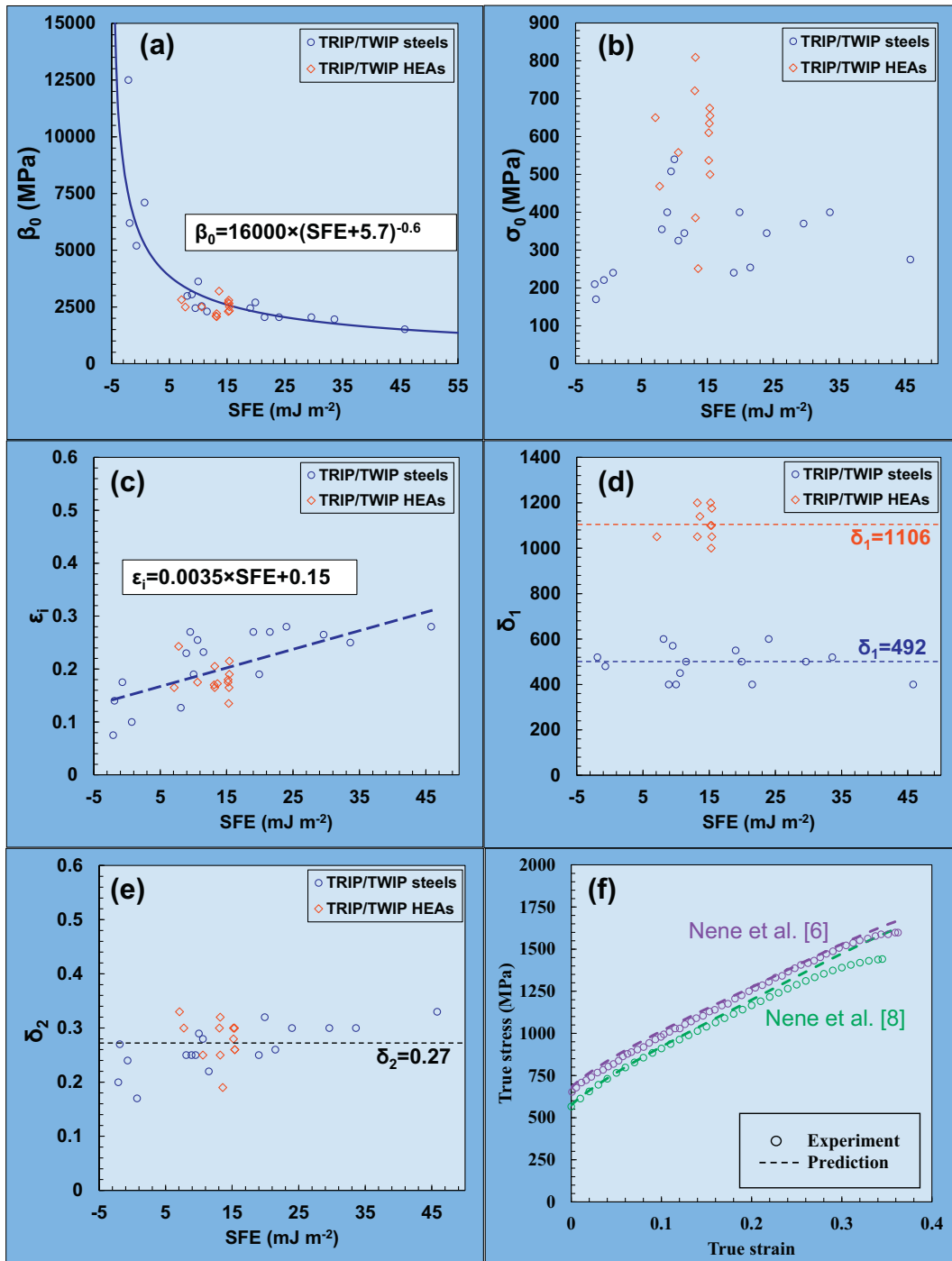


Fig. 8 – Correlation of the work hardening model parameters as function of SFE obtained for TRIP HEAs [5–8] and TRIP/TWIP steels [11,39–43], (a) β_0 , (b) σ_0 , (c) ε_i , (d) δ_1 , (e) δ_2 , and (f) comparison of model prediction with experiments using correlation of work hardening model parameters as a function of SFE.

strongly on effective SFE of the alloy and hence justify the trend in Fig. 8 (a). Parameter δ_1 controls the rate of drop in work hardening in Stages I and III as evident from Fig. 4 (a1). When the variation of δ_1 is plotted as a function of SFE (Fig. 8 (d)), data points indicated separate clustering for TRIP HEAs and TRIP/TWIP steels. Data points for TRIP HEAs clustered at a higher δ_1 compared to TRIP/TWIP steels (Fig. 8 (d)). Larger value of δ_1

implies profuse Stage I work hardening as well as gradual drop in work hardening rate due to the onset of martensitic transformation during early deformation stage. Although δ_1 lacks a trend with SFE, an average value of $\delta_1 = 1106$ and $\delta_1 = 492$ fits reasonably well for all TRIP HEAs and TRIP/TWIP steels, respectively. Parameter δ_2 controls the slight increment in hardening during Stage II deformation (Fig. 8 (e)). Similar to

δ_1 , parameter δ_2 also lacks a trend with SFE (Fig. 8 (e)). However, unlike δ_1 , variation in δ_2 with SFE did not show any separate clustering of data points for TRIP HEAs and TRIP steels (Fig. 8 (d)). An average value of $\delta_2 = 0.27$ fitted reasonably well for all alloys summarized in Table 2. Among all model parameters, σ_0 indicated the least trend with SFE (Fig. 8 (b)), as yielding of material is influenced by multiple parameters such as grain size [9], processing route [6,47], presence of secondary phases [47], and initial phase fraction [5].

5.4. Validation of model using correlation of model parameters with SFE

Correlation of the model parameters with SFE for TRIP HEAs and TRIP/TWIP steels reported in literature is used to validate the work hardening model given in Eqns. (1) and (2). For model validation, two TRIP HEAs not included in parametric correlation with SFE in Fig. 8 were used. Due to lack of correlation of with SFE, σ_0 needs to be determined by other means. Nene et al. [8] reported the Hall-Petch relationship (Eqn. (9)) for Cu-HEA where the coefficients were determined to be $\sigma_k = 470$ MPa and $k_y = 271$ MPa,

$$\sigma_0 = \sigma_k + \frac{k_y}{\sqrt{d}} \quad (9)$$

After FSP, the average grain size, d , was obtained as 6.57 μm for S350 condition [8]. Substituting the values of σ_k , k_y , and d in Eqn. (9), the value of σ_0 is obtained as 576 MPa. Using Eqn. (8), effective SFE of Cu-HEA with an average grain size of 6.57 μm was obtained as 10.6 mJ m^{-2} , which is used in the regression fit equations for β_0 and ϵ_i (Fig. 8 (a, c)). Further, a similar methodology was also used for another TRIP HEA having a composition Fe₃₉Mn₂₀Co₂₀Cr₁₅Si₅Al₁ (Al-HEA) [6]. Although Hall-Petch coefficients were not determined for the alloy, an average value of $\sigma_0 = 680$ MPa fitted well for multiple microstructures obtained after FSP and subsequent annealing heat treatment [6], which is used for validation. Average grain size reported for the microstructure is 0.8 μm which yielded a SFE value of 15.3 mJ m^{-2} according to Eqn. (8). As mentioned in Section 6.2, due to lack of trends in δ_1 and δ_2 with SFE, the average values of $\delta_1 = 1106$ and $\delta_2 = 0.27$, which fit reasonably well for all TRIP HEAs, were used for validation. Table 3 provides the numerical values of the correlated model parameters obtained using the value of effective SFE. Figure 8 (f) shows the fits obtained using the correlation of model parameters with SFE and the initial microstructure for Cu-HEA [8] and Al-HEA [6]. Model results fit reasonably well with the experimental values, and confirm the present work hardening model to be an effective tool to predict the tensile stress-strain response of TRIP HEAs as a function of SFE.

Table 3 – Work hardening model parameters obtained from their correlation with SFE for the experimental data sets shown in Fig. 8 (f).

Reference	SFE (mJ m^{-2})	σ_0 (MPa)	β_0 (MPa)	ϵ_i	δ_1	δ_2
[8]	10.6	575	2757	0.19	1106	0.27
[6]	15.3	680	2575	0.20	1106	0.27

6. Summary and conclusions

Work hardening response of metastable TRIP HEAs under tensile deformation that undergoes γ (f.c.c) to ϵ (h.c.p) martensitic transformation encompasses three deformation stages; Stage I deformation characterized by a rapid drop in work hardening rate, Stage II hardening characterized by a gradual rise in work hardening rate, and Stage III hardening characterized by a rapid drop in work hardening rate. Excellent work hardening reported in TRIP HEAs is due to deformation twinning in the transformed martensitic phase in addition to sustained γ (f.c.c) to ϵ (h.c.p) martensitic transformation. Overall work hardening response in TRIP HEAs under tensile deformation, which reflects the hardening due to synergistic activity of multiple deformation mechanisms, is modeled using a five-parameter work hardening model. Some of the model parameters identified for TRIP HEAs and TRIP/TWIP steels reported in literature correlated well with their SFE. The trend of the model parameters with SFE was used to validate the work hardening model; reasonably good fit justified the possibility of work hardening model as a function of SFE to be used as a predictive tool to determine the mechanical response in TRIP HEAs.

Data availability statement

The raw/processed data required to reproduce these findings cannot be shared at this time as the data also forms part of an ongoing study.

Declaration of Competing Interest

The authors declare that they have no known competing financial interests or personal relationships that could have appeared to influence the work reported in this paper.

Acknowledgments

The present work was performed under the cooperative agreement between the Army Research Laboratory (ARL) and the University of North Texas (W911NF-18-2-0067). Authors acknowledge Materials Research Facility at University of North Texas for access to scanning electron microscopy and transmission electron microscopy. Authors are also grateful to Dr. Jeffrey T. Lloyd for his valuable suggestions.

Appendix A. Supplementary data

Supplementary data to this article can be found online at <https://doi.org/10.1016/j.jmrt.2022.04.016>.

REFERENCES

- [1] Yeh JW, Chen SK, Lin SJ, Gan JY, Chin TS, Shun TT, et al. Nanostructured high-entropy alloys with multiple principal

- elements: novel alloy design concepts and outcomes. *Adv Eng Mater* 2004;6:299–303. <https://doi.org/10.1002/adem.200300567>.
- [2] Zhang Y, Ting T, Tang Z, Gao MC, Dahmen KA, Liaw PK, et al. Progress in materials science microstructures and properties of high-entropy alloys. *J. Prog. Mater. Sci.* 2014;61:1–93. <https://doi.org/10.1016/j.pmatsci.2013.10.001>.
- [3] Agrawal P, Haridas RS, Thapliyal S, Yadav S, Mishra RS, McWilliams BA, et al. Metastable high entropy alloys: an excellent defect tolerant material for additive manufacturing. *Mater Sci Eng* 2021;826:142005. <https://doi.org/10.1016/j.msea.2021.142005>.
- [4] Li Z, Pradeep KG, Deng Y, Raabe D, Tasan CC. Metastable high-entropy dual-phase alloys overcome the strength–ductility trade-off. *Nature* 2016;534:227–30. <https://doi.org/10.1038/nature17981>.
- [5] Nene SS, Liu K, Frank M, Mishra RS, Brennan RE, Cho KC, et al. Enhanced strength and ductility in a friction stir processing engineered dual phase high entropy alloy. *Sci Rep* 2017;7:16167. <https://doi.org/10.1038/s41598-017-16509-9>.
- [6] Nene SS, Sinha S, Frank M, Liu K, Mishra RS, McWilliams BA, et al. Unexpected strength–ductility response in an annealed, metastable, high-entropy alloy. *Appl Mater Today* 2018;13:198–206. <https://doi.org/10.1016/j.apmt.2018.09.002>.
- [7] Nene SS, Frank M, Liu K, Sinha S, Mishra RS, McWilliams B, et al. Reversed strength–ductility relationship in microstructurally flexible high entropy alloy. *Scripta Mater* 2018;154:163–7. <https://doi.org/10.1016/j.scriptamat.2018.05.043>.
- [8] Nene SS, Frank M, Liu K, Sinha S, Mishra RS, McWilliams BA, et al. Corrosion-resistant high entropy alloy with high strength and ductility. *Scripta Mater* 2019;166:168–72. <https://doi.org/10.1016/j.scriptamat.2019.03.028>.
- [9] Nene SS, Frank M, Liu K, Mishra RS, McWilliams BA, Cho KC. Extremely high strength and work hardening ability in a metastable high entropy alloy. *Sci Rep* 2018;8:9920. <https://doi.org/10.1038/s41598-018-28383-0>.
- [10] Mishra RS, Haridas RS, Agrawal P. High entropy alloys – tunability of deformation mechanisms through integration of compositional and microstructural domains. *Mater Sci Eng* 2021;812:141085. <https://doi.org/10.1016/j.msea.2021.141085>.
- [11] Allain S, Chateau JP, Bouaziz O, Migot S, Guelton N. Correlations between the calculated stacking fault energy and the plasticity mechanisms in Fe-Mn-C alloys. *Mater Sci Eng* 2004;387–389:158–62. <https://doi.org/10.1016/j.msea.2004.01.059>.
- [12] Kibey S, Liu JB, Johnson DD, Sehitoglu H. Predicting twinning stress in fcc metals: linking twin-energy pathways to twin nucleation. *Acta Mater* 2007;55:6843–51. <https://doi.org/10.1016/j.actamat.2007.08.042>.
- [13] Olson GB, Cohen M. A general mechanism of martensitic nucleation: Part I. General concepts and the FCC → HCP transformation. *Metall Trans A* 1976;7:1897–904. <https://doi.org/10.1007/BF02659822>.
- [14] Arsenlis A, Parks DM. Crystallographic aspects of geometrically-necessary and statistically-stored dislocation density. *Acta Mater* 1999;47:1597–611. [https://doi.org/10.1016/S1359-6454\(99\)00020-8](https://doi.org/10.1016/S1359-6454(99)00020-8).
- [15] Estrin Y, Tóth LS, Molinari A, Bréchet Y. A dislocation-based model for all hardening stages in large strain deformation. *Acta Mater* 1998;46:5509–22. [https://doi.org/10.1016/S1359-6454\(98\)00196-7](https://doi.org/10.1016/S1359-6454(98)00196-7).
- [16] Galindo-Navia EI, Rivera-Díaz-del-Castillo PEJ. Understanding martensite and twin formation in austenitic steels: a model describing TRIP and TWIP effects. *Acta Mater* 2017;128:120–34. <https://doi.org/10.1016/j.actamat.2017.02.004>.
- [17] Bouaziz O, Moon J, Kim HS, Estrin Y. Isotropic and kinematic hardening of a high entropy alloy. *Scripta Mater* 2021;191:107–10. <https://doi.org/10.1016/j.scriptamat.2020.09.022>.
- [18] Stringfellow RG, Parks DM, Olson GB. A constitutive model for transformation plasticity accompanying strain-induced martensitic transformations in metastable austenitic steels. *Acta Metall Mater* 1992;40:1703–16. [https://doi.org/10.1016/0956-7151\(92\)90114-T](https://doi.org/10.1016/0956-7151(92)90114-T).
- [19] Papatriantafyllou I, Agoras M, Aravas N, Haidemenopoulos G. Constitutive modeling and finite element methods for TRIP steels. *Comput Methods Appl Mech Eng* 2006;195:5094–114. <https://doi.org/10.1016/j.cma.2005.09.026>.
- [20] Lloyd JT, Field DM, Limmer KR. A four parameter hardening model for TWIP and TRIP steels. *Mater Des* 2020;194. <https://doi.org/10.1016/j.matdes.2020.108878>.
- [21] Haridas RS, Agrawal P, Mishra RS. Modeling the work hardening behavior in metastable high entropy alloys. *Mater Sci Eng* 2021;141778. <https://doi.org/10.1016/j.msea.2021.141778>.
- [22] Sinha S, Nene SS, Frank M, Liu K, Lebensohn RA, Mishra RS. Deformation mechanisms and ductile fracture characteristics of a friction stir processed transformative high entropy alloy. *Acta Mater* 2020;184:164–78. <https://doi.org/10.1016/j.actamat.2019.11.056>.
- [23] Frank M, Chen Y, Nene SS, Sinha S, Liu K, An K, et al. Investigating the deformation mechanisms of a highly metastable high entropy alloy using in-situ neutron diffraction. *Mater Today Commun* 2020;23:100858. <https://doi.org/10.1016/J.MTCOMM.2019.100858>.
- [24] Li Z, Pradeep KG, Deng Y, Raabe D, Tasan CC. Metastable high-entropy dual-phase alloys overcome the strength–ductility trade-off. *Nature* 2016;534:227–30. <https://doi.org/10.1038/nature17981>.
- [25] Mishra RS, Nene SS, Frank M, Sinha S, Liu K, Shukla S. Metastability driven hierarchical microstructural engineering: overview of mechanical properties of metastable complex concentrated alloys. *J Alloys Compd* 2020;842:155625. <https://doi.org/10.1016/j.jallcom.2020.155625>.
- [26] Mishra RS, Nene SS. Some unique aspects of mechanical behavior of metastable transformative high entropy alloys. *Metall Mater Trans* 2021;52:889–96. <https://doi.org/10.1007/s11661-021-06138-3>.
- [27] Nene SS, Frank M, Agrawal P, Sinha S, Liu K, Shukla S, et al. Microstructurally flexible high entropy alloys: linkages between alloy design and deformation behavior. *Mater Des* 2020;194:108968. <https://doi.org/10.1016/j.matdes.2020.108968>.
- [28] Mishra RS, Ma ZY. Friction stir welding and processing. *Mater Sci Eng R Rep* 2005;50:1–78. <https://doi.org/10.1016/j.mser.2005.07.001>.
- [29] Zhang T, Zhao RD, Wu FF, Lin SB, Jiang SS, Huang YJ, et al. Transformation-enhanced strength and ductility in a FeCoCrNiMn dual phase high-entropy alloy. *Mater Sci Eng* 2020;780. <https://doi.org/10.1016/j.msea.2020.139182>.
- [30] Jo YH, Choi WM, Kim DG, Zargaran A, Sohn SS, Kim HS, et al. FCC to BCC transformation-induced plasticity based on thermodynamic phase stability in novel V 10 Cr 10 Fe 45 Co x Ni 35–x medium-entropy alloys. *Sci Rep* 2019;9:1–14. <https://doi.org/10.1038/s41598-019-39570-y>.
- [31] Agrawal P, Shukla S, Gupta S, Agrawal P, Mishra RS. Friction stir gradient alloying: a high-throughput method to explore the influence of V in enabling HCP to BCC transformation in a γ-FCC dominated high entropy alloy. *Appl Mater Today* 2020;21:100853. <https://doi.org/10.1016/j.apmt.2020.100853>.

- [32] Sinha S, Nene SS, Frank M, Liu K, Agrawal P, Mishra RS. On the evolving nature of c/a ratio in a hexagonal close-packed epsilon martensite phase in transformative high entropy alloys. *Sci Rep* 2019;9:1–14. <https://doi.org/10.1038/s41598-019-49904-5>.
- [33] Haridas RS, Agrawal P, Thapliyal S, Yadav S. Strain rate sensitive microstructural evolution in a TRIP assisted high entropy alloy : experiments , microstructure and modeling. *Mech Mater* 2021;156:103798. <https://doi.org/10.1016/j.mechmat.2021.103798>.
- [34] Bu Y, Li Z, Liu J, Wang H, Raabe D, Yang W. Nonbasal slip systems enable a strong and ductile hexagonal-close-packed high-entropy phase. *Phys Rev Lett* 2019;122:75502. <https://doi.org/10.1103/PhysRevLett.122.075502>.
- [35] Yoo MH. Slip, twinning, and fracture in hexagonal close-packed metals. *Metall Trans A* 1981;12:409–18. <https://doi.org/10.1007/BF02648537>.
- [36] Thapliyal S, Nene SS, Agrawal P, Wang T, Morphew C, Mishra RS, et al. Damage-tolerant, corrosion-resistant high entropy alloy with high strength and ductility by laser powder bed fusion additive manufacturing. *Addit Manuf* 2020;36:101455. <https://doi.org/10.1016/j.addma.2020.101455>.
- [37] Agrawal P, Thapliyal S, Nene SS, Mishra RS, McWilliams BA, Cho KC. Excellent strength-ductility synergy in metastable high entropy alloy by laser powder bed additive manufacturing. *Addit Manuf* 2020;32:101098. <https://doi.org/10.1016/j.addma.2020.101098>.
- [38] Laplanche G, Kostka A, Horst OM, Eggeler G, George EP. Microstructure evolution and critical stress for twinning in the CrMnFeCoNi high-entropy alloy. *Acta Mater* 2016;118:152–63. <https://doi.org/10.1016/j.actamat.2016.07.038>.
- [39] Field DM, Qing J, Van Aken DC. Chemistry and properties of medium-Mn two-stage TRIP steels. *Metall. Mater. Trans. A Phys. Metall. Mater. Sci.* 2018;49:4615–32. <https://doi.org/10.1007/s11661-018-4798-6>.
- [40] Buchely MF, Field DM, Van Aken DC. Analysis of hot- and cold-rolled loads in medium-Mn TRIP steels. *Metall Mater Trans B Process Metall Mater Process Sci* 2019;50:1180–92. <https://doi.org/10.1007/s11663-019-01566-4>.
- [41] De Cooman BC, Kwon O, Chin KG. State-of-the-knowledge on TWIP steel. *Mater Sci Technol* 2012;28:513–27. <https://doi.org/10.1179/1743284711Y.0000000095>.
- [42] Hwang JK. Revealing the small post-necking elongation in twinning-induced plasticity steels. *J Mater Sci* 2020;55:8285–302. <https://doi.org/10.1007/s10853-020-04477-x>.
- [43] Yin FX, Xia H, Feng JH, Cai MH, Zhang X, Wang GK, et al. Mechanical properties of an Fe-30Mn-4Si-2Al alloy after rolling at different temperatures ranging from 298 to 1073 K. *Mater Sci Eng* 2018;725:127–37. <https://doi.org/10.1016/j.msea.2018.03.079>.
- [44] Lu W, Liebscher CH, Dehm G, Raabe D, Li Z. Bidirectional transformation enables hierarchical nanolaminate dual-phase high-entropy alloys. *Adv Mater* 2018;30:1–10. <https://doi.org/10.1002/adma.201804727>.
- [45] Zambrano OA. Stacking fault energy maps of Fe-Mn-Al-C-Si steels: effect of temperature, grain size, and variations in compositions. *J. Eng. Mater. Technol. Trans. ASME* 2016;138:1–9. <https://doi.org/10.1115/1.4033632>.
- [46] Field DM, Van Aken DC. Dynamic strain aging phenomena and tensile response of medium-Mn TRIP steel. *Metall. Mater. Trans. A Phys. Metall. Mater. Sci.* 2018;49:1152–66. <https://doi.org/10.1007/s11661-018-4481-y>.
- [47] Gwalani B, Gorsse S, Choudhuri D, Styles M, Zheng Y, Mishra RS, et al. Modifying transformation pathways in high entropy alloys or complex concentrated alloys via thermo-mechanical processing. *Acta Mater* 2018;153:169–85. <https://doi.org/10.1016/j.actamat.2018.05.009>.